1 **Causes of a continuous summertime O$_3$ pollution event in Ji'nan, a central**

2 **city in the North China Plain**

3 Xiaopu Lyu[1], Nan Wang[2], Hai Guo[1*], Likun Xue[3], Fei Jiang[4], Yangzong Zeren[1], Hairong Cheng

4 [5], Zhe Cai[4], Lihui Han[6], Ying Zhou[6]

5 [1] Air Quality Studies, Department of Civil and Environmental Engineering, The Hong Kong

6 Polytechnic University, Hong Kong, China

7 [2] Division of Environmental Meteorology，Institute of Tropical and Marine Meteorology，

8 China Meteorology Administration，Guangzhou，China

9 [3] Environment Research Institute, Shandong University, Ji'nan, China

10 [4] Jiangsu Provincial Key Laboratory of Geographic Information Science and Technology,

11 International Institute for Earth System Science, Nanjing University, Nanjing, China

12 [5] Department of Environmental Engineering, School of Resource and Environmental Sciences,

13 Wuhan University, Wuhan, China

14 [6] Department of Environmental Science, College of Environmental and Energy Engineering,

15 Beijing University of Technology, Beijing, China

16 * Corresponding author: ceguohai@polyu.edu.hk

17

18 **Abstract:** In summer 2017, measurements of ozone (O$_3$) and its precursors were carried out at an

19 urban site in Ji'nan, a central city in the North China Plain (NCP). A continuous O$_3$ pollution

20 event was captured during August 4-11, with the maximum hourly O$_3$ reaching 154.1 ppbv.

21 Model simulation indicated that local photochemical formation and regional transport

22 contributed 14.0±2.3 and 18.7±4.0 ppbv/hr to the increase of O$_3$ during 09:00-15:00 local time

23 (LT) in this event, respectively. For local O$_3$ formation, the calculated OH reactivities of volatile

24 organic compounds (VOCs) and carbon monoxide (CO) were comparable between O$_3$ episodes

25 and non-episodes ($p > 0.05$), so was the OH reactivity of nitrogen oxides (NO$_x$). However, the

26 ratio of OH reactivity of VOCs and CO to that of NO$_x$ increased from 2.0±0.4 s^{-1}/s^{-1} during non-

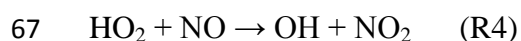27 episodes to 3.7±0.7 s^{-1}/s^{-1} during O$_3$ episodes, which resulted in the change of O$_3$ formation
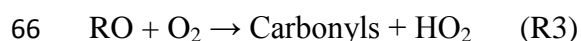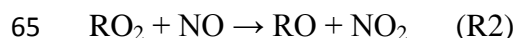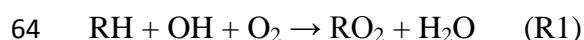
1

28 mechanism from the VOC-limited regime before the O_3 pollution event to the transitional regime

29 during the event. Correspondingly, the simulated local O_3 production rate during the event

30 (maximum: 21.3 ppbv/hr) was markedly higher than that before the event ($p<0.05$) (maximum:

31 16.9 ppbv/hr). Given that gasoline and diesel exhaust made large contributions to the abundance

32 of O_3 precursors and O_3 production rate, constraint on vehicular emissions is the most effective

33 strategy to control O_3 pollution in Ji'nan. The NCP has been confirmed as a source region of

34 tropospheric O_3, where the shift of regimes controlling O_3 formation like the case presented in

35 this study can be expected across the entire region, due to the substantial reductions of NO_x

36 emissions in recent years.

37 **Keywords:** Ozone, local formation, regional transport, volatile organic compound, North China

38 Plain

39 **1 Introduction**

40 Air pollution in the North China Plain (NCP), the largest alluvial plain of China consisting of

41 Beijing, Tianjin and many cities in Hebei, Shandong, and Henan provinces, has attracted much

42 attention in recent years. While the annual average concentration of $PM_{2.5}$ (particulate matters

43 with aerodynamic diameter less than or equal to 2.5 μm) has been reduced under concerted

44 efforts on emission restrictions (Zhang et al., 2015; Lang et al., 2017), the tropospheric ozone

45 (O_3) pollution, which is less visible than haze but may be equivalently harmful to human health,

46 is still severe. At a regional receptor site of the NCP in a mountainous area to the north of

47 Beijing, Wang et al. (2006) reported the maximum hourly O_3 of 286 ppbv. A year-round

48 observation of O_3 at 10 urban sites in Beijing indicated frequent O_3 non-attainments (hourly $O_3 >$

49 100 ppbv) through May to August of 2013 (Wang et al., 2015a). Hourly O_3 mixing ratio of up to

50 120 ppbv was reported on Mt. Tai, the highest mountain in the NCP (1534 m a.s.l.) (Gao et al.,

51 2005). All these studies revealed the significant photochemical O_3 pollution over the entire NCP.

52 Moreover, O_3 has been increasing in the NCP during the last decades (Zhang et al., 2014; Zhang

53 et al., 2015). The increase rate of O_3 at an urban site in Beijing from 2005 to 2011 was quantified

54 as 2.6 ppbv/year (Zhang et al., 2014), comparable to that (1.7-2.1 ppbv/year) at Mt. Tai in the

55 summer between 2003 and 2015 (Sun et al., 2016). Overall, the NCP suffers from severe O_3

56 pollution, which is even aggravating.

57   Apart from the intrusion of stratospheric O_3 in some places with high elevations (Cooper et al.,

58   2005; Lin et al., 2015), photochemical formation is the main source of the ground-level O_3.

59   Volatile organic compounds (VOCs), carbon monoxide (CO) and nitrogen oxides (NO_x) are key

60   precursors of tropospheric O_3 (Crutzen, 1973; Chameides and Walker, 1973; Carter, 1994; Carter

61   et al., 1995). The general chemical reactions R(1) - R(5) show the production of O_3 from the OH

62   initiated oxidation of hydrocarbons (RH) (Jenkin et al., 1997; Atkinson, 2000; Jenkin and

63   Clemitshaw, 2000).

64    $RH + OH + O_2 \rightarrow RO_2 + H_2O$ (R1)

65    $RO_2 + NO \rightarrow RO + NO_2$ (R2)

66    $RO + O_2 \rightarrow Carbonyls + HO_2$ (R3)

67    $HO_2 + NO \rightarrow OH + NO_2$ (R4)

68    $NO_2 + O_2 + hv \rightarrow O_3 + NO$ (R5)
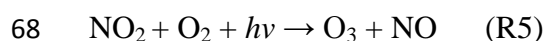
69   The production of O_3 is generally limited by VOCs or NO_x or co-limited by both VOCs and NO_x,

70   depending upon the chemical compositions of the air, particularly the ratio between OH

71   reactivity of VOCs and NO_x (OH reactivity is the sum of the products of O_3 precursors

72   concentrations and the reaction rate constants between O_3 precursors and OH). Xue et al. (2014)

73   indicated that the formation of O_3 was limited by NO_x in Lanzhou in summer, consistent with the

74   findings of Liu et al. (2010) who proved that NO_x-limited regime dominated O_3 formation in

75   most areas of northwestern China. In southwestern China, O_3 formation was diagnosed as VOC-

76   limited in Chengdu, but NO_x-limited in Pengzhou due to the large amount of emissions from

77   petrochemical industry (Tan et al., 2018a). Lyu et al. (2016) reported the VOC-limited regime in

78   Wuhan, central China. The VOC-limited regime has also been repeatedly confirmed for O_3

79   formation in Shanghai (Xue et al., 2014; Xing et al., 2017) and Nanjing (Ding et al., 2013),

80   eastern China. In the Pearl River Delta of southern China, it was found that O_3 formation was

81   generally limited by VOCs in the southwest, while limited by NO_x in the northeast (Ye et al.,

82   2016). In the NCP, both Han et al. (2018) and Xing et al. (2018) summarized that VOCs limited

83   the production of O_3 in most urban areas. However, in the suburban and rural areas, O_3 formation

84   was generally in the transitional regime, *e.g.* Yucheng (Zong et al., 2018), or limited by NO_x, *e.g.*

85   Wangdu (Tan et al., 2018b). From a historical perspective, Jin et al. (2017) pointed out that the

86   sensitivity of O_3 formation to VOCs increased in most Chinese cities, however decreased in

87 some megacities (such as Beijing and Shanghai) due to the stringent control of NO_x emissions in

88 recent years. Different VOCs play non-equivalent roles in O_3 formation. Alkenes, aromatics and

89 carbonyls can be readily oxidized by oxidative radicals (*e.g.* OH) or photolyzed (applicable for

90 carbonyls), leading to O_3 formation (Cheng et al., 2010; Guo et al., 2013). Therefore, the sources

91 with large quantities of emissions of these VOCs generally make considerable contributions to

92 the photochemical production of ground-level O_3. For example, Cheng et al. (2010) pointed out

93 that carbonyls increased the peak O_3 production rates at a rural site and at a suburban site in

94 South China by 64% and 47%, respectively. Solvent based industry and paint solvent usage with

95 intensive emissions of aromatics were responsible for more than half of O_3 formation potential in

96 Shanghai (Cai et al., 2010). Carbonyls and alkenes accounted for 71-85% of the total OH

97 reactivity of VOCs in Beijing (Shao et al., 2009).

98 In addition to the chemical processes, meteorological conditions also play significant roles in the

99 formation, transport and accumulation of O_3. Studies (Chan and Chan, 2000; Huang et al., 2005)

100 indicated that tropical cyclone (typhoon as the mature form) and continental anticyclone are the

101 most common synoptic systems conducive to O_3 pollution in coastal cities of South China. Many

102 O_3 episodes in East China occurred under the control of the west Pacific subtropical high

103 pressure (He et al., 2012; Shu et al., 2016). In the NCP (North China), the summertime O_3

104 pollution is generally accompanied with weak high pressure systems (Wang et al., 2010).

105 Furthermore, O_3 pollution is also related to the topography. For example, the mountains to the

106 north and west of Beijing lead to upslope winds (valley breeze) in daytime, which transport the

107 polluted air masses laden with O_3 and/or O_3 precursors from the NCP to Beijing (Lin et al.,

108 2008). Overall, the causes of O_3 pollution are complicated and need to be analyzed case by case.

109 The NCP is the region with the largest emissions of many air pollutants, such as VOCs and NO_x,

110 in China (Gu et al., 2014; Li et al., 2017), partially accounting for the severe O_3 pollution there.

111 In addition, O_3 pollution in the NCP is closely related to the synoptic systems and topographic

112 features (Chen et al., 2009; Zhang et al., 2016). For example, the strong photochemical

113 production of O_3 in urban plumes of Beijing was found by Wang et al. (2006), while the

114 contribution of regional transport was revealed by the enhanced O_3 production at a rural site in

115 the NCP under southerly winds (Lin et al., 2008). Through the review of synoptic systems in the

116 NCP from 1980 to 2013, Zhang et al. (2016) concluded that the air quality was generally

117 unhealthy under weak East Asian Monsoons. Moreover, a decadal statistical analysis indicated

118 that meteorological factors explained ~50% of the O_3 variations in Beijing (Zhang et al., 2015).

119 Despite many previous studies, the evolutions of the synoptic and photochemical processes in O_3

120 pollution events and their contributions to the non-attainment of O_3 have been seldom looked

121 into in the NCP. Besides, the local and regional contributions to the elevated O_3 in the NCP are

122 not unambiguously quantified, limited by the deficiencies in model representation of either

123 physical or local chemical processes. The situation was even much worse for Ji'nan, the capital

124 of Shandong province. As early as 2000s, studies (Shan et al., 2008; Yin et al., 2009) reported

125 the maximum hourly O_3 of 143.8 ppbv and 147.8 ppbv in June 2004 and 2005, respectively.

126 Even higher O_3 (198 ppbv) was observed at a rural site downwind of Ji'nan in June 2013 (Zong

127 et al., 2018). However, almost no study was carried out to explore the mechanisms responsible

128 for high O_3 there, though it has been confirmed that air pollution in the cities like Ji'nan in the

129 NCP influenced air quality in Beijing (Lin et al., 2008; Wang et al., 2010). To better understand

130 O_3 pollution in the NCP, this study investigated the causes of an O_3 episode event lasting for

131 eight days in Ji'nan in summer 2017. The analyses presented here focused on the synoptic

132 systems dominating Shandong Peninsula during this event; the chemical profiles of O_3 and O_3

133 precursors; and the simulation of factors contributing to O_3 in Ji'nan with the aid of a chemical

134 transport model and a photochemical box model. In addition, we proposed feasible O_3 control

135 measures based on the source-resolved OH reactivity of VOCs and NO_x.

136 **2 Methodology**

137 **2.1 Site description**

138 The air quality monitoring and sample collection were carried out on the rooftop of a 7-story

139 building on the campus of Shandong University from July 15 to August 14, 2017. The campus is

140 located in the urban area of Ji'nan, and the site is about 50 m from a main road (Shanda South

141 Road) outside the campus. Figure 1 shows the locations of the sampling site (36.68 °N, 117.07 °E,

142 22 m a.g.l.) and the surrounding air quality monitoring stations (AQMSs) set up by China

143 National Environmental Monitoring Center (CNEMC). Also shown are the observed O_3 and

144 rainfall averaged over August 4-11, 2017 when the O_3 episode event occurred in Ji'nan. It is

145 noteworthy that the days with maximum hourly O_3 exceeding 100 ppbv (Grade II of National

146 Ambient Air Quality Standard) were defined as O_3 episode days. The hourly O_3 values at the

147 AQMSs were obtained from the website of CNEMC (http://www.cnemc.cn/). The high O_3 levels

148 at almost all the AQMSs in the NCP (Figure 1 (a)) indicated a regional O_3 pollution event in this

149 period. In view of the comparable O_3 mixing ratios observed at our sampling site to those at the

150 surrounding AQMSs, we believe that the observations at our sampling site to some extent

151 represented the characteristics of this regional pollution event. This was confirmed by the strong

152 influences of regional transport on O_3 variations at the site, as discussed in section 3.3.
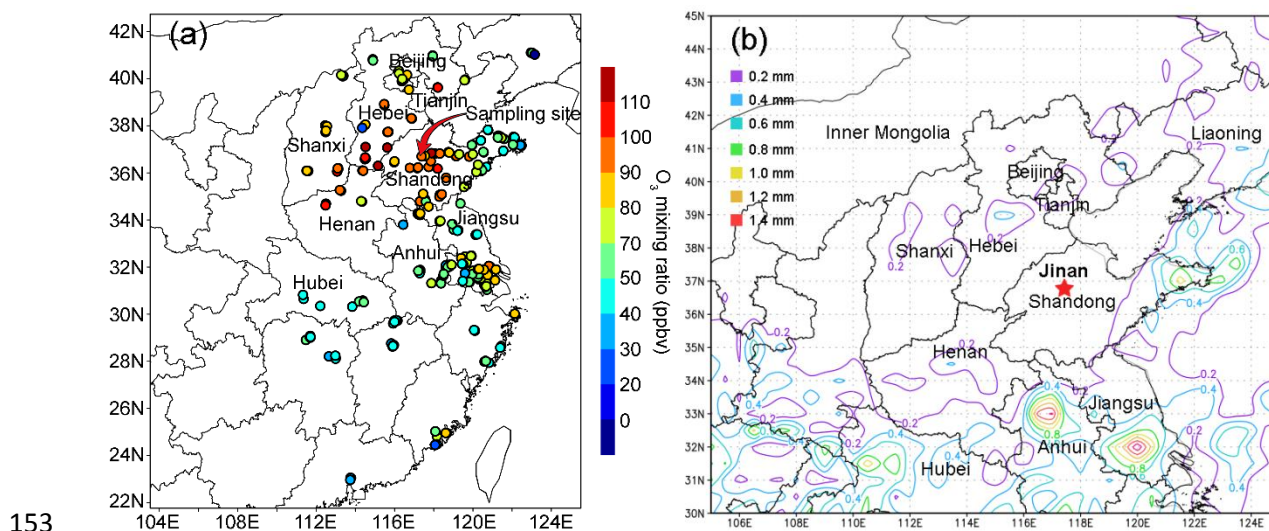
153

154 Figure 1 (a) Locations of the sampling site and the CNEMC AQMSs, and the average observed

155 O_3 at 14:00 LT on August 4-11, 2017 (colored circles). The sampling site is overlapped with the

156 nearest AQMS in Ji'nan. (b) Rainfall distribution, in millimeters (mm), averaged over August 4-

157 11, 2017.

2.2 Air quality monitoring and sample collection

2.2.1 Continuous monitoring of air pollutants and meteorological parameters

160 O_3, NO and NO_2 were continuously monitored at the sampling site between July 15 and August

161 14, 2017. The air was drawn through a 4 m Teflon tube by the built-in pumps of the trace gas

162 analyzers at the total flow rate of 2 L/min (1.4 L/min for O_3 analyzer and 0.6 L/min for NO_x

163 analyzer). The inlet was located ~1 m above the rooftop of the building. O_3 and NO/NO_x were

164 detected with a UV photometric based analyzer and a chemiluminescence NO-NO_2-NO_x

165 analyzer, respectively (see Table S1 for the specifications). The lowest NO observed during the

166 sampling period was 2.4 ppbv, 6 times the detection limit (DL) of the NO_x analyzer (0.4 ppbv).

6

167   Since the measurement accuracy of the analyzer was <15%, the DL was low enough to not
168   influence the accurate measurements of NO in this study. NO_2 was calculated from the
169   difference between NO and NO_x. Studies indicated that NO_2 monitored with chemiluminescence
170   was generally overestimated due to the conversion of the total odd nitrogen (NO_y) to NO by
171   molybdenum oxide catalysts (McClenny et al., 2002; Dunlea et al., 2007; Xu et al., 2013). The
172   positive bias was more significant in more aged air masses, resulting from higher levels of NO_z
173   ($NO_z = NO_y - NO_x$) (Dunlea et al., 2007). The average overestimation of NO_2 was 22% in
174   Mexico City, which even increased to 50% in the afternoon (Dunlea et al., 2007). Xu et al. (2013)
175   suggested that the chemiluminescence monitors overestimated NO_2 by less than 10% in urban
176   areas with fresh emission of NO_x, but the positive bias went up to 30-50% at the suburban sites.
177   As described in section 2.1, our sampling site was located in the urban area of Ji'nan and was
178   only ~50 m to a main road. Therefore, we infer that NO_2 might not be significantly
179   overestimated in this study. However, larger overestimation could be expected during O_3
180   episodes, when the stronger photochemical reactions caused higher production of NO_z.
181   According to Xu et al. (2013), we adopted 30% (minimum bias in suburban area) and 10%
182   (maximum bias in urban area) as the maximum fraction of NO_2 overestimation during episodes
183   and non-episodes at this urban site, respectively. The influences of the NO_2 measurement
184   interferences on the results were discussed where necessary.

185   The hourly concentrations of sulfur dioxide (SO_2) and CO were acquired from a nearest AQMS,
186   which is ~1 km from our sampling site. Year-round monitoring of inorganic trace gases was
187   conducted at this AQMS. The air was drawn into the analyzers at a flow of 3 L/min through an
188   inlet, ~1 m above the rooftop of a 5-story building (~ 16 m a.g.l.). The specifications of the
189   analyzers deployed at the AQMS are also provided in Table S1. The hourly concentrations of O_3
190   and NO_2 measured at the AQMS (NO data was not available at the CNEMC website) agreed
191   well with those observed at our sampling site, with the slope of 1.04 ($R^2 = 0.82$) and 1.13 ($R^2 =$
192   0.71) for O_3 and NO_2 in the linear least square regressions, respectively (Figure S1). Due to the
193   differences in analyzers and/or in sources and sinks of air pollutants between the two sites, the
194   agreements were worse at low mixing ratios for both O_3 and NO_2. Therefore, we only used SO_2
195   and CO monitored at the AQMS in this study, which had lower photochemical reactivity than O_3
196   and NO_2, and were more homogeneous at a larger scale.

197 In addition, the meteorological parameters, including wind speed, wind direction, pressure,
198 temperature and relative humidity, were monitored at the sampling site by a widely used weather
199 station (China Huayun group, Model CAWS600-B). The daily total solar radiation was obtained
200 from the observations at a meteorological station in Ji'nan (36.6 $^\circ$N, 117.05 $^\circ$E, 170.3 m a.s.l), 9
201 km to our sampling site.

2.2.2 Sample collection and chemical analysis

203 The VOC and oxygenated VOC (OVOC) samples were collected on 9 selective days (*i.e.*, July
204 20 and 30, August 1, 4-7 and 10-11), referred to as VOC sampling days hereafter. The days were
205 selected to cover the periods with relatively high and normal levels of O_3. The high O_3 days were
206 forecasted prior to sampling based on the numerical simulations of meteorological conditions
207 and air quality. In total, 6 out of 9 VOC sampling days were O_3 episode days with the maximum
208 hourly O_3 values ranging from 100.4 to 154.1 ppbv. On each day (regardless of episode or non-
209 episode), 6 VOC/OVOC samples were collected between 08:00 and 18:00 LT every 2 hours with
210 the duration of 1 hour for VOC and 2 hours for OVOC samples. VOC samples were collected
211 with 2 L stainless steel canisters which were cleaned and evacuated before sampling. A flow
212 restrictor was connected to the inlet of the canister to guarantee 1 hour sampling. OVOC were
213 sampled with the 2,4-dinitrophenylhydrazine (DNPH) cartridge, in front of which an O_3 scrubber
214 was interfaced to remove O_3 in the air. A pump was used to draw the air through the DNPH
215 cartridge at a flow of 500 mL/min. After sampling, all the DNPH cartridges were stored in a
216 refrigerator at 4 $^\circ$C till chemical analysis.

217 VOC samples were analyzed with a gas chromatograph-mass selective detector/flame ion
218 detector/electron capture detector system (Colman et al., 2001). In total, 85 VOCs, including 59
219 hydrocarbons, 19 halocarbons and 7 alkyl nitrates, were quantified. The overall ranges of the DL,
220 accuracy and precision for VOCs analysis were 1-154 pptv, 1.2-19.8% and 0.1-17.9%,
221 respectively. The analysis results given by this system have been compared with those analyzed
222 by UCI and good agreements were achieved (Figure S2). OVOC samples were eluted with 5 mL
223 acetonitrile, followed by analysis with the high performance liquid chromatography. The DL,
224 accuracy and precision for the detected OVOCs species were within the range of 3-11 pptv, 0.32-
225 0.98% and 0.01-1.03%, respectively.

2.3 Model configuration

2.3.1 Chemical transport model

To analyze the processes contributing to high O_3 in Ji'nan, a chemical transport model, i.e. the Weather Research Forecast-Community Multi-scale Air Quality (WRF-CMAQ), was utilized to simulate O_3 in this study. WRF v3.6.1 was run to provide the offline meteorological field for CMAQ v5.0.2. A two-nested domain was adopted with the resolution of 36 km (outer domain) and 12 km (inner domain), respectively. As shown in Figure S3, the outer domain covered the entire continental area of China aiming to provide sufficient boundary conditions for the inner domain, which specifically focused on eastern China.

We used the 2012-based Multi-resolution Emission Inventory for China (MEIC) to provide anthropogenic emissions of air pollutants, which was developed by Tsinghua University specific for China, with the grid resolution of $0.25\,°×0.25\,°$ (Zhang et al., 2007; He, 2012). Five emission sectors, namely transportation, agriculture, power plant, industry and residence were included in MEIC. The emission inventory was linearly interpolated to the domains with consideration of the earth curvature effect. For grids outside China, the air pollutant emissions were derived from INTEX-B (Intercontinental Chemical Transport Experiment-Phase B) Asian emission inventory (Zhang et al., 2009). Consistent with many previous studies (Jiang et al., 2010; Wang et al., 2015b), the Model of Emissions of Gases and Aerosols from Nature (MEGAN) was used to calculate the biogenic emissions. The physical and chemical parameterizations for WRF-CMAQ were generally identical to those described in Wang et al. (2015b), with the following improvements. Firstly, the carbon bond v5 with updated toluene chemistry (CB05-TU) was chosen as the gas phase chemical mechanism (Whitten et al., 2010). Secondly, a single-layer urban canopy model (Kusaka and Kimura, 2004) was used to model the urban surface-atmosphere interactions. Thirdly, the default 1990s U.S. Geological Survey data in WRF was replaced by adopting the 2012-based moderate resolution imaging spectroradiometer (MODIS) land cover data for eastern China. The substitution was performed to update the simulation of boundary meteorological conditions (Wang et al., 2007).

An integrated process rate (IPR) module incorporated in CMAQ was used to analyze the processes influencing the variations of O_3. Through solving the mass continuity equation established between the overall change of O_3 concentration across time and the change of O_3 concentration caused by individual processes, including horizontal diffusion (HDIF), horizontal

257 advection (HADV), vertical diffusion (VDIF), vertical advection (VADV), dry deposition
258 (DDEP), net effect of chemistry (CHEM) and cloud processes (CLD), the O_3 variation rates
259 induced by individual processes were determined. Note that since the estimate of CHEM is
260 influenced by the estimate of O_3 precursor emissions, the simulation of meteorological
261 conditions and the chemical mechanism, all the three aspects should be taken into account
262 wherever CHEM is discussed. The IPR analysis has been widely applied in diagnosis of
263 processes influencing O_3 pollution (Huang et al., 2005; Wang et al., 2015b). Since the field
264 observations were conducted near the surface (~ 22 m a.g.l.), and the box model (section 2.3.2)
265 was constrained by the observations, the modeling results on the ground-level layer were
266 extracted from WRF-CMAQ for analyses in this study.

2.3.2 Photochemical box model

268 We also utilized a Photochemical Box Model incorporating the Master Chemical Mechanism
269 (PBM-MCM) to study the in situ O_3 chemistry, thanks to the detailed (species-based)
270 descriptions of VOC degradations in the MCM (Saunders et al., 2003; Lam et al., 2013). The
271 PBM model was localized to be applicable in Ji'nan, with the settings of geographic coordinates,
272 sunlight duration and photolysis rates. The photolysis rates were calculated by the TUV model
273 (Madronich and Floke, 1997). Specifically, the geographical coordinates, date and time were
274 input into the TUV model to initialize the calculation of solar radiation with the default aerosol
275 optical depth (AOD), cloud optical depth (COD), surface albedo and other parameters. Then,
276 COD was adjusted to make the calculated daily total solar radiation progressively approach the
277 observed value. When the difference between the calculated and observed solar radiation was
278 less than 1%, the input parameters with the adjusted COD were accepted. Based on the settings,
279 the hourly solar radiations and the photolysis rates of O_3 ($J(O^1D)$) and NO_2 (JNO_2) were
280 calculated by the TUV model, and applied to the PBM-MCM for O_3 chemistry modelling. Table
281 S2 shows the daily maximum $J(O^1D)$ and JNO_2 on the VOC sampling days. The MCM v3.2
282 (http://mcm.leeds.ac.uk/MCM/) consists of 17,242 reactions among 5,836 species. The mixing
283 ratios of O_3 and its precursors at 00:00 on each day were used as the initial conditions for each
284 day's modelling. The initial O_3 therefore represented O_3 left over from the days before the
285 modelling day, and partially accounted for the primary OH production. Hourly concentrations of
286 46 VOCs, 4 OVOCs and 4 trace gases (SO_2, CO, NO and NO_2), as well as hourly meteorological

287 parameters (temperature and relative humidity) were taken as inputs to constrain the model. O_3,

288 as the species to be modeled, was not input except for the setting of initial conditions. The Freon,

289 cycloalkanes and methyl cycloalkanes with low O_3 formation potentials were not included in

290 model inputs either. Also excluded were the species whose concentrations were lower than the

291 DLs in more than 20% samples, such as the methyl hexane and methyl heptane isomers. For the

292 hours when measurement data were not available, the concentrations were obtained with linear

293 interpolation. Some secondary species, such as formaldehyde (HCHO), acetaldehyde and

294 acetone, were input into the model to constrain the simulation. Since other secondary species,

295 *e.g.*, PAN and HNO_3 were not observed in this study, their concentrations were calculated by the

296 model. The model simulated dry depositions of all the chemicals, and the deposition velocities

297 were set identical to those in Lam et al. (2013). Since NO and NO_2 were separately measured,

298 they were not treated as a whole (i.e. NO_x) in the model. Instead, both NO and NO_2 data were

299 input into the model so that the partitioning between them was constrained to observations.

300 The simulations were separately performed on all the VOC sampling days. As spin-up, the model

301 was run 72 hours prior to the simulation on the day of interest, with the same inputs. The model

302 treated the air pollutants to be well-mixed within the boundary layer, while dilution and transport

303 were not considered. O_3 in the free troposphere was not considered either, due to the lack of O_3

304 observations above the boundary layer over Ji'nan. This might hinder the accurate reproduction

305 of the observed O_3, particularly on the days when advection and diffusion were strong. Since the

306 model mainly described the in situ photochemistry, it was validated through comparison with the

307 CHEM process simulated by WRF-CMAQ. The simulated O_3 production rates were output every

308 hour, which were integrated values over every 3600 s in one hour (model resolution: 1 s). More

309 details about the model configuration can be found in Lam et al. (2003) and Lyu et al. (2017).

310 **3. Results and discussion**

311 **3.1 Overall characteristics of O_3 pollution in Ji'nan**

312 Figure 2 shows the time series of trace gases, OH reactivity of VOCs, CO and NO_x, and

313 meteorological conditions on the VOC sampling days in Ji'nan (Trace gases in the whole

314 sampling period are shown in Figure S4). All the OH reactivity values discussed in this study

315 were calculated rather than observed ones. The OH reactivity of VOCs was categorized into

316 carbonyls, biogenic VOCs (BVOCs), aromatics, alkenes and alkanes (Table S3 lists the VOCs

317 included in each group). The reaction rate constants between O_3 precursors and OH in

318 calculation of OH reactivity were adopted from the MCM v3.2. The average total OH reactivity

319 on all the VOC sampling days (19.4 ± 2.1 s^{-1}) was comparable to that reported in New York (19 ± 3

320 s^{-1}, Ren et al., 2003), Houston (9-22 s^{-1}, Mao et al., 2010) and Beijing (15-27 s^{-1}, Williams et al.,

321 2016). Consistent with previous studies in urban areas (Ren et al., 2003; Yang et al., 2016 and

322 references therein), NO_x was the largest contributor ($28.9 \pm 1.9\%$) to the total OH reactivity.

323 Noticeably, $20.5 \pm 4.1\%$ of the total OH reactivity were attributable to BVOCs, which were much

324 higher than the contributions in urban areas ($<10\%$) reviewed by Yang et al. (2016). The

325 elevated isoprene levels (2.2 ± 0.6 ppbv during episodes and 0.9 ± 0.3 ppbv during non-episodes)

326 under high temperature (mean: 31 $^\circ$C) explained the considerable contribution of BVOCs to the

327 total OH reactivity in this study.

328 The total OH reactivity of VOCs and CO ($OH\ reactivity_{VOCs+CO}$) was comparable between O_3

329 episodes (14.8 ± 2.0 s^{-1}) and non-episodes (12.2 ± 3.0 s^{-1}), so was the OH reactivity of NO_x

330 (4.7 ± 0.8 s^{-1} and 6.9 ± 1.9 s^{-1} during episodes and non-episodes, respectively). Taking the positive

331 biases of NO_2 measurement into account (section 2.2.1), we found that the OH reactivity of NO_x

332 was overestimated at maximum by $17.5 \pm 1.1\%$ and $5.4 \pm 0.7\%$ during O_3 episodes and non-

333 episodes, respectively. In the case of maximum overestimation, the actual OH reactivity of NO_x

334 during episodes (4.0 ± 0.7 s^{-1}) might be lower ($p<0.05$) than that during non-episodes (6.6 ± 1.9 s^{-1}).

335 The high OH reactivity during non-episodes mainly occurred on July 30 and August 1, due to the

336 unfavorable meteorological conditions, which were discussed later. Despite the comparable OH

337 reactivity, we found that the ratio of $\frac{OH\ reactivity_{VOCs+CO}}{OH\ reactivity_{NOx}}$ during O_3 episodes (3.7 ± 0.7 s^{-1}/s^{-1}) was

338 higher than during non-episodes (2.0 ± 0.4 s^{-1}/s^{-1}) ($p<0.05$). The difference was likely even larger,

339 due to the more significant overestimation of NO_2 during episodes. This indicated that O_3

340 formation was more limited by VOCs during non-episodes than during episodes. Indeed, O_3

341 formation in Ji'nan switched from the VOC-limited regime during non-episodes to the

342 transitional regime during episodes (see section 3.4.2). This partially explained the build-up of

343 O_3 on episode days, because the transitional regime features the highest O_3 production rates.

344 From the aspect of meteorological conditions, O_3 episodes had relatively stronger solar radiation,

345 higher temperature, lower relative humidity and weaker winds ($p<0.05$). This is reasonable as O_3

346 formation and accumulation are generally enhanced under these weather conditions. In particular,

the solar radiation on July 30 was much weaker than those during O_3 episodes, primarily accounting for the low O_3 on this day. Figure S5 shows the COD retrieved from the terra/MODIS (https://ladsweb.modaps.eosdis.nasa.gov/search/imageViewer/1/MOD06_L2--61/2017-08-06/DB/Site:142/2873994172--3) at 10:00 – 12:00 LT on all the VOC sampling days. The terra/MODIS image revealed thick cloud cover with high COD over Ji'nan on July 30, which caused the weak solar radiation. The influences of cloud cover/COD and solar radiation on O_3 pollution were further discussed in section 3.2. Unlike our previous understanding that O_3 pollution is aggravated under high pressure (Chan and Chan, 2000; Zhao et al., 2009), the sea-level pressure during O_3 episodes (993.4±0.2 hPa) was significantly lower than during non-episodes (996.1±0.4 hPa) in this study ($p<0.05$). When O_3 reached its hourly maximum on August 10 (154.1 ppbv), the pressure was at its lowest value (990.2 hPa). This discrepancy inspired us to look into the synoptic and chemical processes in this continuous O_3 pollution event.
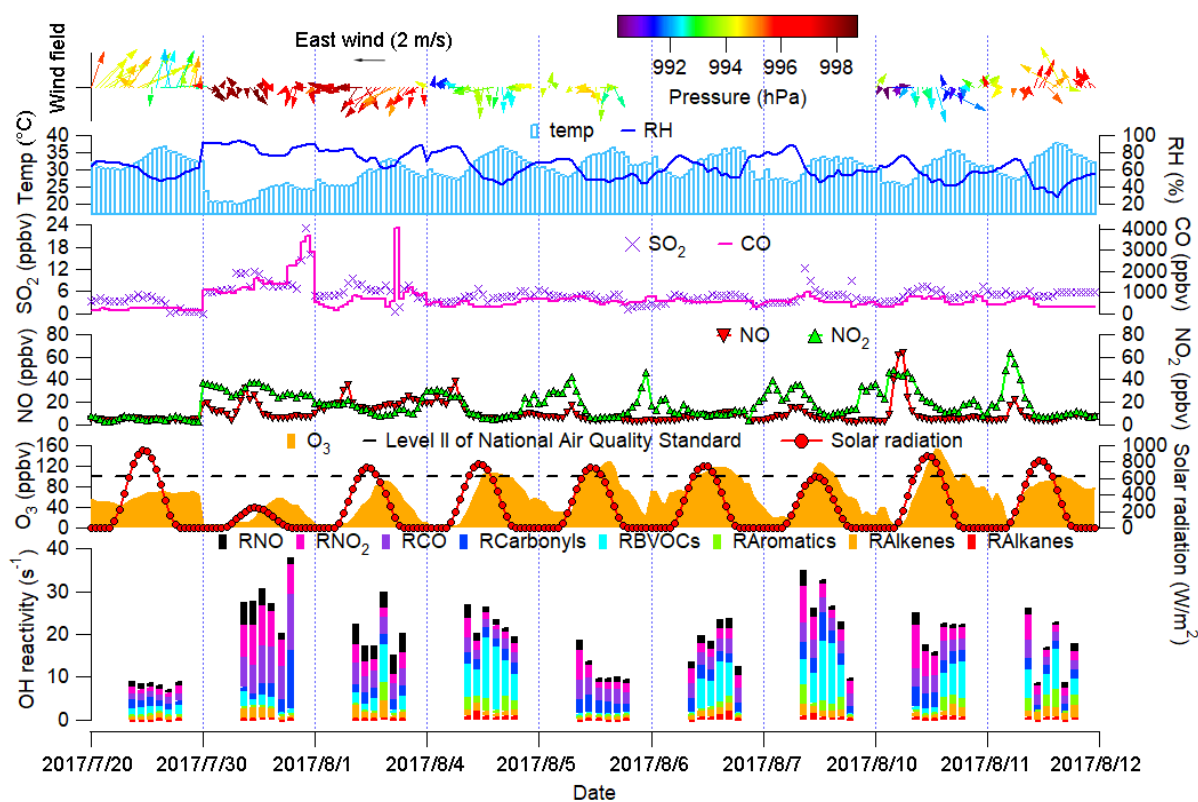
Figure 2 Time series of trace gases, OH reactivity of O_3 precursors and meteorological parameters. Wind speed and wind direction were not monitored from 17:00 LT on August 5 to 23:00 LT on August 7 due to malfunction of the weather station. RX in the bottom panel is the OH reactivity of species/group X.

13

3.2 Synoptic processes and relationship with O_3 pollution

Figure 3 displays the average weather charts at 14:00 LT during O_3 episodes and non-episodes (weather charts on individual VOC sampling days are shown in Figure S6). Clearly, the temperature in Shandong province was much higher during O_3 episodes than non-episodes, which favored O_3 formation on episode days. Additionally, southerly and southwesterly winds originating from the inland areas (Hubei, Henan, and Anhui provinces) prevailed in central and western Shandong during O_3 episodes. In contrast, the winds were generally from the sea or coastal regions in Jiangsu province during non-episodes. It is more likely that O_3 and O_3 precursors were transported to Ji'nan during episodes. The high concentrations of O_3 precursors on July 30 and August 1 (non-episode days) were mainly caused by the weather conditions (high pressure, low temperature and low solar radiation), as discussed in section 3.1. Further, we also noticed that the winds changed direction from the southwest to the northwest around Ji'nan during O_3 episodes. This meant that there might be a local circulation, hampering the dispersion of air pollutants during episodes. It seemed that the change of wind direction was caused by the convergence of continental air and sea breeze from Bohai Bay, similar to the convergence zone formed over the Pearl River Estuary in South China (Fung et al., 2005; Lo et al., 2006). Overall, the surface winds were more favorable for regional transport and accumulation of air pollutants during O_3 episodes. In addition, Shandong province was under the control of a uniform pressure system with the sea-level pressure of 1000-1001 hPa during O_3 episodes, implying the relatively stagnant weather.
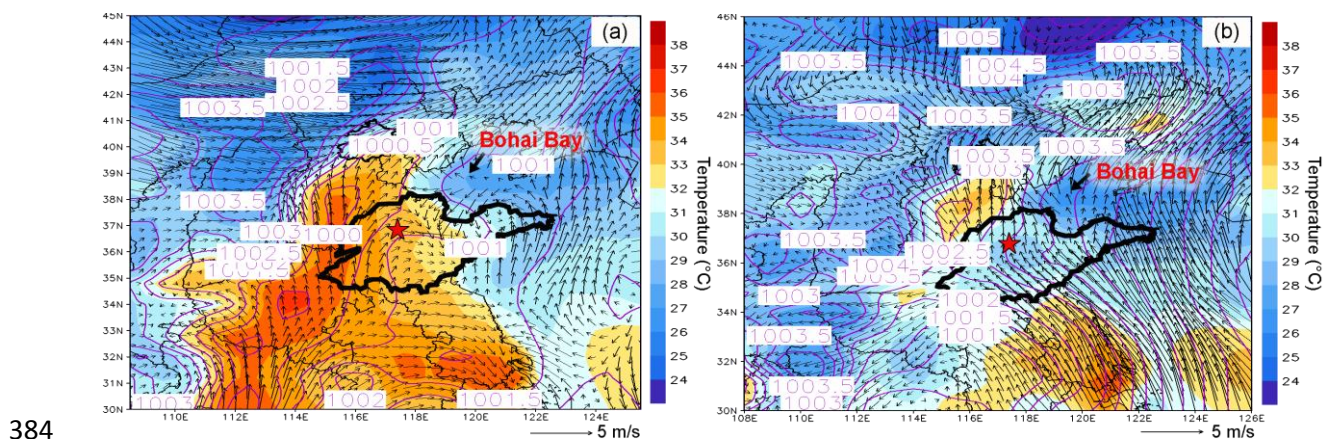

Figure 3 Weather chart at 14:00 LT averaged over (a) O_3 episodes and (b) non-episodes. The red star represents Ji'nan. The dark black line is the boundary of Shandong province. Bohai Bay is

387 located to the northeast of Shandong province. Numbers in the figure are sea-level pressures in
388 unit of hPa.

389 To better understand the relationship between O_3 pollution and the synoptic systems, Table 1
390 summarizes the synoptic systems, weather conditions and air mass origins on all the VOC
391 sampling days. The weather charts at surface level and 500 hPa on August 1, 4, 7, 10 and 13 are
392 presented in Figures S7-S8, showing the evolution of the synoptic systems. To identify the
393 origins of air masses, the backward trajectories of air masses are shown in Figure 4. The
394 trajectories were computed using the Hybrid Single Particle Lagrangian Integrated Trajectory
395 (HYSPLIT) Model v 4.9. Each trajectory was calculated for 48 hours and the calculation was
396 done every 6 hours (4 trajectories each day). Our sampling site (36.68 °N, 117.07 °E) was set as
397 the end point of the trajectories with the height of 500 m a.s.l. The discrepancy between the wind
398 direction and origin of air masses, *e.g.* on August 1 and 11, was likely due to the air recirculation
399 at the ground level.

400 It was found that Ji'nan was under the control of the Western Pacific Subtropical High (WPSH)
401 on July 20 (weather chart on 500 hPa is not shown here), and the air masses arriving in Ji'nan
402 originated from South China (Figure 4). As anticipated, the WPSH caused high temperature and
403 the intensive solar radiation (Figure 2), which was conducive to O_3 formation. However, the
404 winds on July 20 were the strongest in the entire VOC sampling period, with the highest hourly
405 wind speed of 3.9 m/s. The strong winds facilitated the dispersion of O_3 and its precursors,
406 leading to low O_3 levels on this day. The WPSH moved southward on the following days and
407 Ji'nan was controlled by a uniform pressure system, which was formed in the peripheries of two
408 low pressure systems (two rain belts as shown in Figure 1), *i.e.* one over Central China and
409 another over North China (Figure S7). Thus, the pressure in Ji'nan was relatively high
410 (997.1±0.3 hPa), compared to the south and north regions. This synoptic system lasted for
411 several days until August 7, covering 2 non-episode days and 4 O_3 episode days. The low O_3 on
412 2 non-episode days (July 30 and August 1) were mainly attributable to the weak solar radiation
413 and low temperature as discussed above.

414 In contrast, continuously strong solar radiations with low COD (Figure 2 and Figure S5), high
415 temperature and continental air masses (Figure 4) were observed on August 4-7. This, in addition
416 to the shift of O_3 formation mechanism (see sections 3.1 and 3.4.2), explained the prolonged O_3

pollution event. On August 10, the rain belt over North China moved southward, forming a deep low pressure trough over the NCP and Ji'nan was behind the trough (Figure S8 (d)). The low pressure trough is a typical synoptic system conducive to O_3 pollution, resulting from the intrusion of O_3 in the stratosphere and/or the upper troposphere (Chan and Chan, 2000). Moreover, there was nearly no cloud cover over the entire NCP on August 10 (Figure S5). Consequently, the highest O_3 (154.1 ppbv) in this sampling campaign was observed. On August 11, the low pressure system continued to extend to the Yellow Sea. O_3 decreased substantially on this day with the disappearance of the low pressure trough and the weakening of solar radiation, though the hourly maximum O_3 still reached 100.4 ppbv. On the following days, the precipitations relieved the O_3 pollution in Ji'nan.

Table 1 Summary of the synoptic systems, weather conditions and air mass origins on VOC sampling days.

| Date	Maximum hourly O_3 (ppbv)	Episode/non-episode	Synoptic system Weather condition	Air mass origin
July 20	71.0	Non-episode	WPSH, strong southwesterly winds	Continental air masses from South China
July 30	57.6		Uniform pressure field (weak high pressure), rain, fog, calm winds	Marine air masses
August 1	90.6		Uniform pressure field (weak high pressure), northeasterly winds	
August 4	107.5	Episode	Uniform pressure field (weak high pressure), northeasterly winds	Continental air masses from Shandong province
August 5	128.2		Uniform pressure field (weak high pressure), calm winds	
August 6	116.9		Uniform pressure field (weak high pressure), southwesterly winds	
August 7	126.9		Uniform pressure field (weak high pressure), calm winds	Continental air masses from the north
August 10	154.1		Low-pressure trough, calm winds	Continental air masses from the west

| August 11 | 100.4 | | Subtropical high, southeasterly winds | Continental air masses from the southwest |

429


430
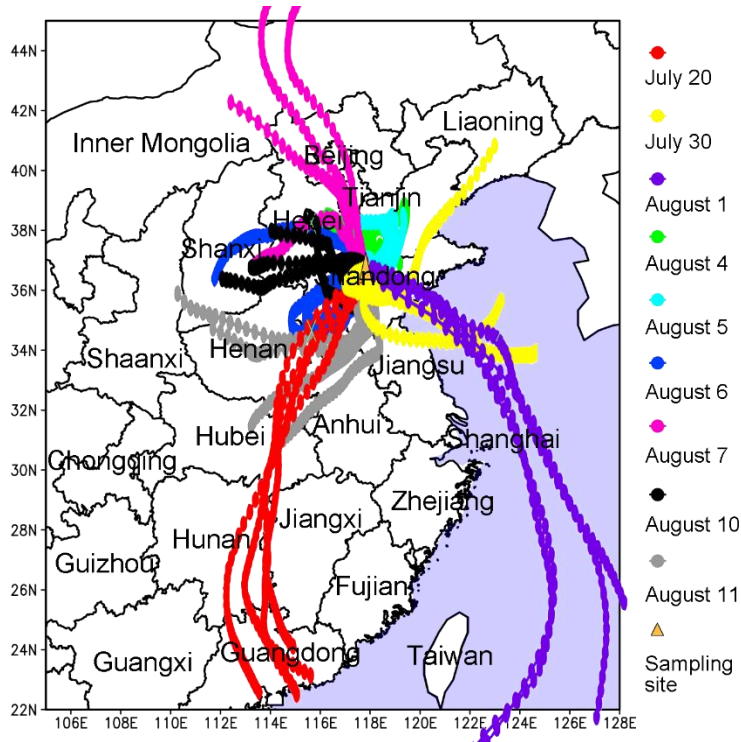
Figure 4 Forty eight hour backward trajectories calculated every 6 hours, with Ji'nan (36.68 N, 117.07 E, 500 m a.g.l.) as the ending point. The trajectories are simulated by HYSPLIT v4.9. The water areas are highlighted in blue.

3.3 O$_3$ simulation and process analysis

The observations indicated the likely different regimes controlling local O$_3$ formation and the potential impacts of regional transport. To understand the atmospheric chemistry and dynamics, as well as their roles in this O$_3$ pollution event, the WRF-CMAQ was applied. Figure 5 shows the hourly average simulated and observed O$_3$ on the VOC sampling days in Ji'nan. Overall, the model well reproduced the magnitudes and diurnal patterns of the observed O$_3$, except for the higher simulated O$_3$ on July 20 and the under-prediction of O$_3$ on August 1, 7 and 10. Discussions on the discrepancies and the model validation were provided in Text S1, Figures S9-S11 and Table S4.

17

443
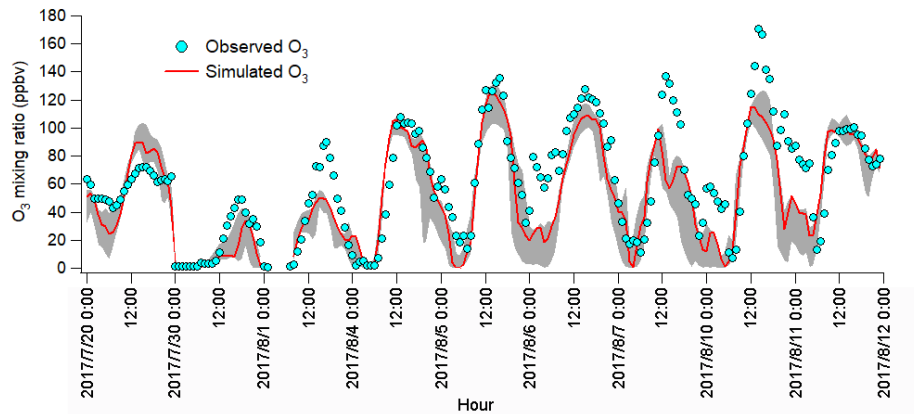
Figure 5 Hourly average mixing ratios of the WRF-CMAQ simulated and observed O_3 in Ji'nan.
The grey area shows the minimum and maximum simulated O_3 at the sampling site and 8
adjoining grids (12×12 km^2 for each grid).

The IPR analysis quantified the O_3 variation rates induced by different processes, as shown in
Figure 6. HDIF and HADV were summed as horizontal transport (HTRA), and the vertical
transport (VTRA) was a total representative of VDIF and VADV. It was found that chemical
reactions generally led to the decrease of O_3 mixing ratio during non-episodes. The negative
contributions of chemical reactions on July 20 coincided with the very low concentrations of O_3
precursors and the flat diurnal cycle of O_3 (Figure 2). The chemical destruction to O_3 on July 30
and August 1 was most likely related to the weak solar radiation and low temperature, which
inhibited the photochemical reactions. In fact, the negative chemical effect should be considered
as the titration of NO to the regionally-transported and/or background O_3 and the depletion of O_3
by the freshly emitted NO near the sources (Beck and Grennfelt, 1994; Sillman, 1999).
Conversely, the combined effect of horizontal and vertical transport was to increase O_3 levels
during non-episodes.

During O_3 episodes, chemical reactions made positive contributions to O_3 production rates
between 09:00 LT and 15:00 LT, with the average hourly O_3 production rate of 14.0 ± 2.3 ppbv/hr.
At the same time, O_3 was also elevated by transport at an average rate of 18.7 ± 4.0 ppbv/hr, as a
combined effect of vertical transport (-40.8 ± 20.2 ppbv/hr) and horizontal transport (59.5 ± 19.8
ppbv/hr). The negative contribution of vertical transport to O_3 in these hours might be caused by
the updraft with the increase of temperature in the city. The positive contributions of horizontal
transport could be explained by the air masses laden with O_3 originating from the west and the

18

north (Figure 4 and Figure S10). The much higher O_3 over the NCP than in the surrounding regions indicated that the NCP was an O_3 source in this case. In fact, the transport of O_3 from the lower troposphere over the NCP to the free troposphere and further to northeast China was also presented by Ding et al. (2009).

During 16:00-08:00 LT on O_3 episode days, O_3 was titrated and chemically consumed at the rate of 49.4±6.3 ppbv/hr. This was reasonable, because the fresh vehicular emissions in the morning and evening rush hours consumed O_3, particularly the irreversible titration of NO to O_3 in absence of sunlight. The NO_2 produced from the titration reaction was carried over to the other places by air circulation, and/or oxidized to NO_3 and N_2O_5, which could further react with aerosol to form HNO_3 and $ClNO_2$ in the evening. Horizontal and vertical transport dominated O_3 sources, with the average positive contribution of 5.7±7.0 and 54.5±9.6 ppbv/hr during 16:00-08:00 LT on August 4-11, respectively. The strong vertical transport coincided with the downward winds in the evening, which brought the high-altitude O_3 to the ground, as indicated in Figure S9. However, the sources of O_3 in the upper atmosphere were beyond the scope of this study.
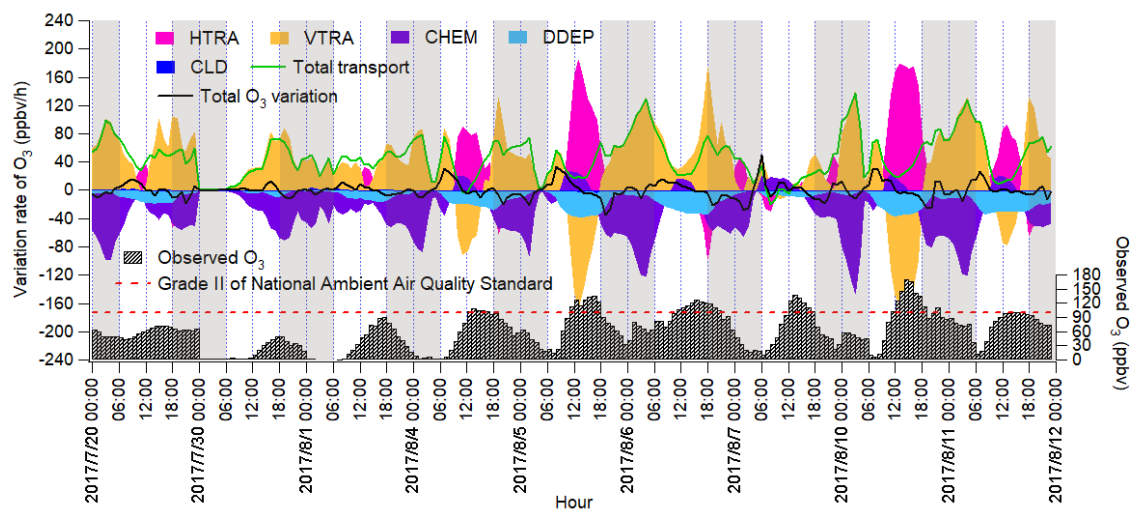
Figure 6 Time series of O_3 variation rate in Ji'nan induced by individual processes calculated based on the change of O_3 per hour. Total transport is the sum of HTRA and VTRA, and the sum of O_3 variation rates attributable to all the processes is represented by total O_3 variation rate. The nighttime (18:00 – 06:00 LT) has been highlighted in grey.

3.4 Local O_3 formation and control

3.4.1 Pathway and source contributions to O_3 production

The IPR analyses showed that chemical reactions served as an important source of O_3 on episode days in Ji'nan, particularly during 09:00-15:00 LT when O_3 was at high levels. This process was further studied through the simulation of the in-situ photochemistry by PBM-MCM. It should be noted that the simulations were based on the observed concentrations of O_3 precursors, which could be influenced by both local and regional air. It required cautions to extend the results to all the situations in Ji'nan, because the regional effect was not always consistent. Table S5 lists the production and destruction pathways of O_3 (Thornton et al., 2002; Monks, 2005; Kanaya et al., 2009). Briefly, the oxidation of NO by HO_2 and RO_2 produced NO_2, which led to O_3 formation following NO_2 photolysis (R2 and R4-R5 in introduction). Therefore, the reactions between NO and HO_2/RO_2 were considered as the production pathways of O_3. To account for O_3 destruction, reaction between $O^1(D)$ and H_2O denoted the photolysis of O_3, and reactions of O_3 with OH, HO_2 and alkenes were also included. Furthermore, since HNO_3 was an important sink of NO_2, the reaction between OH and NO_2 was treated to be destructive to O_3. The titration of O_3 by NO was not included in O_3 destruction, because NO_2 produced in this reaction was either not considered as a source of O_3.

Figure 7 (a) and (b) show the average diurnal cycles of the simulated contributions to O_3 production rates of different pathways. Also shown are the net O_3 production rates simulated by PBM-MCM (*O_3 production $_{PBM-MCM}$*), those simulated by WRF-CMAQ (*O_3 production $_{CHEM}$*), and those calculated from the observed hourly O_3 (*O_3 production $_{obs.}$*). Overall, *O_3 production $_{PBM-MCM}$* and *O_3 production $_{obs.}$* were on the same magnitudes, especially during O_3 episodes with more stagnant weather conditions. This indicated that the PBM-MCM model reasonably reproduced the in situ O_3 photochemistry. Though obvious discrepancies existed between *O_3 production $_{CHEM}$* and *O_3 production $_{PBM-MCM}$*, they agreed well with each other during 10:00-15:00 LT on episode days, consistent with the finding that chemical reactions made great contributions to O_3 in these hours (Figure 6). The lower or even negative *O_3 production $_{CHEM}$* resulted from the titration of the regionally transported and/or local background O_3 by NO and the following depletion of NO_2 through reacting with OH and/or dispersion. Differently, PBM-MCM did not consider the transport of O_3, though the transport effect was partially represented by constraining the model to the observed concentrations of O_3 precursors. In addition, the PBM-MCM was constructed by

20

517 the observed air pollutants, which were already subject to chemical reactions before being
518 detected by the analytical instruments. This meant that the reaction between NO and O_3 from the
519 emission to the detection of NO_x was not considered in PBM-MCM. However, as an emission-
520 based model, WRF-CMAQ performed better in describing the reactions immediately after the
521 emissions of air pollutants. Therefore, the chemical destructions of O_3 in the vicinity of NO_x
522 sources also accounted for the aforementioned discrepancy. The obviously higher reaction rates
523 between NO and O_3 simulated by WRF-CMAQ (Figure S12) confirmed our inferences.

524 During both O_3 episodes and non-episodes, the reaction between HO_2 and NO dominated over
525 "RO_2+NO" in O_3 production, while the O_3 destruction was mainly attributable to the formation
526 of HNO_3, the reaction between O_3 and HO_2 and photolysis of O_3. The net O_3 production rate
527 during O_3 episodes (maximum: 21.3 ppbv/hr) was much ($p < 0.05$) higher than during non-
528 episodes (maximum: 16.9 ppbv/hr), which partially explained the higher O_3 on episode days. In
529 general, "OH+NO_2" serves as the chain terminating reaction in VOC-limited regime of O_3
530 formation, while the radical-radical reactions take over the role in NO_x-limited regime
531 (Finlayson-Pitts and Pitts, 1993; Kleinman, 2005). Here, we found that the ratio of total reaction
532 rates between "HO_2+RO_2" and "OH+NO_2" substantially increased from 0.2±0.1 during non-
533 episodes to 1.0±0.3 during O_3 episodes ($p < 0.05$). This suggested that O_3 formation during non-
534 episodes was limited by VOCs, while it switched to be co-limited by VOCs and NO_x during O_3
535 episodes in view of the equivalent role of "HO_2+RO_2" and "OH+NO_2" in terminating the chain
536 reactions.

537
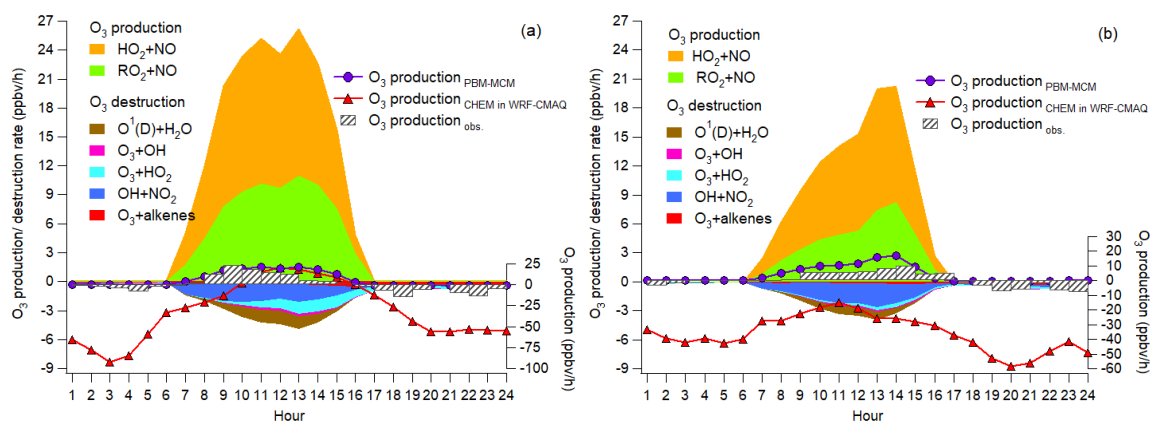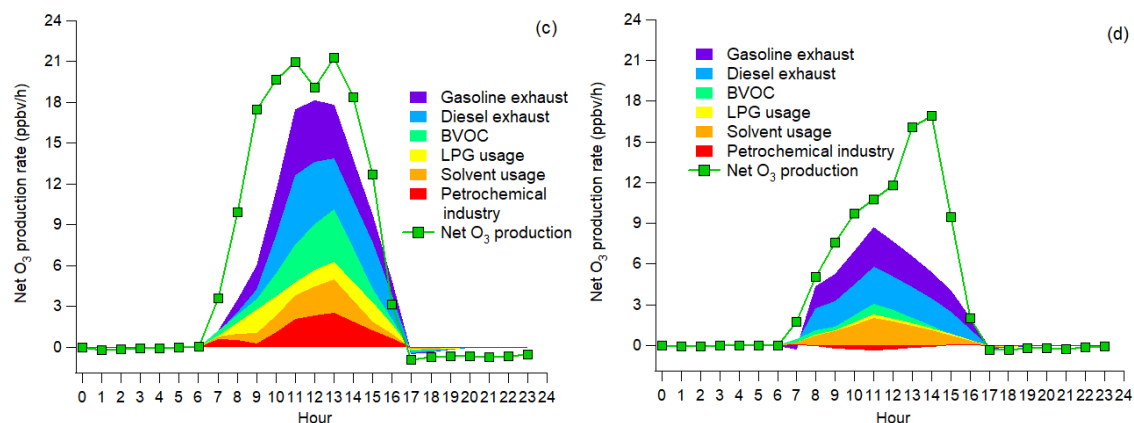
Figure 7 Pathway contributions to O_3 production and destruction rate during episodes (a) and non-episodes (b). Contributions of O_3 precursor sources to net O_3 production rate during episodes (c) and non-episodes (d).

Further, the contributions to the net O_3 production rates of different sources of O_3 precursors were identified, as presented in Figure 7 (c) and (d). Text S2 and Figure S13 illustrate the source apportionment of O_3 precursors and the simulations of the source-specific contributions to O_3 production rates. The results are presented in Table 2. Since the source apportionment was performed for the ambient O_3 precursors which were already subject to atmospheric processes, such as dispersion, deposition and chemical reactions, the results represented the source contributions to the steady – state concentrations of O_3 precursors and the corresponding O_3 production rates. It was found that gasoline exhaust and diesel exhaust were the largest contributors to O_3 production rates regardless of O_3 episodes or non-episodes. Further, the net O_3 production rates attributable to gasoline exhaust (diesel exhaust) increased from 1.0 ± 0.3 ppbv/hr (1.0 ± 0.3 ppbv/hr) during non-episodes to 1.8 ± 0.6 ppbv/hr (1.7 ± 0.4 ppbv/hr) during O_3 episodes. This suggested that vehicular emissions played critical roles in building up ground-level O_3 in the O_3 pollution event. If carbonyls were taken into account, the contributions of vehicular emissions to O_3 production rates were even higher than the currently simulated values, due to the abundances of carbonyls in vehicle exhausts (Grosjean et al., 1990; Granby et al., 1997). In addition, the contributions of the other sources to O_3 production rates all increased during O_3 episodes except for solvent usage ($p>0.05$), as listed in Table 2. It is not surprising to see the synchronous increases, because of the stronger solar radiation and higher temperature during episodes.

561 Further insight into the percentage contributions (not shown here) found that the contributions of

562 BVOC, LPG usage and petrochemical industry to O_3 production rates increased substantially

563 from 9.9±4.2%, 4.3±1.4% and -2.8±1.9% during non-episodes to 19.2±4.3%, 9.1±3.4% and

564 12.1±3.1% during O_3 episodes, respectively. The increased O_3 production rates by BVOCs could

565 be explained by the increase of isoprene (episodes: 2.2±0.6 ppbv; non-episodes: 0.9±0.3 ppbv),

566 under higher temperature and stronger solar radiation during O_3 episodes. The enhancement of

567 O_3 production rates driven by petrochemical industry on episode days was likely associated with

568 the dominance of continental air (Figure 4) and the extensive petrochemical industries in the

569 NCP. For example, the mixing ratio of styrene increased from 54.7±22.0 pptv during non-

570 episodes to 162.3±44.7 pptv during O_3 episodes. The reason for elevated O_3 production rates

571 resulting from LPG usage during episodes was unknown. It is worth to note that the source

572 contributions to O_3 production rates might have some uncertainties due to the limited number of

573 samples (54 samples) and O_3 precursors (31 VOCs, CO, NO and NO_2) applied for source

574 apportionment.

575 Table 2 Contributions to VOCs, CO, NO, NO_2 and O_3 production rate by the sources of O_3

576 precursors averaged on the VOC sampling days in Ji'nan (Unit: % unless otherwise specified).

Source	VOCs*	CO	NO	NO_2	O_3 production rate (ppbv/hr)	
					O_3 episodes	Non-episodes
GE [1]	25.7±3.6	29.9±2.1	30.9±2.4	22.2±2.4	1.8±0.6	1.0±0.3
DE [2]	17.6±2.4	57.3±5.2	52.0±5.8	54.4±5.8	1.7±0.4	1.0±0.3
BVOC	6.1±2.6	0.0±1.7	0.0±2.8	0.0±2.3	1.2±0.5	0.2±0.1
LPG [3]	14.7±2.0	2.2±1.1	9.1±1.6	4.7±0.9	0.8±0.5	0.1±0.1
Solvent [4]	17.1±3.9	3.1±1.8	5.1±3.8	7.8±3.1	0.8±0.5	0.7±0.3
PI [5]	18.8±3.1	7.4±1.9	2.9±1.8	10.9±2.5	1.0±0.3	-0.1±0.1

577 VOCs*: VOCs applied in source apportionment (see Text S2).

578 [1] gasoline exhaust, [2] diesel exhaust, [3] LPG usage, [4] solvent usage and [5] petrochemical industry.

579 **3.4.2 O_3 control measures**

580 Both WRF-CMAQ and PBM-MCM revealed the significant local O_3 formation in the O_3

581 pollution event. The relationships between O_3 and its precursors needed to be clarified, so that

582 the science-based control measures could be taken. Throughout the VOC sampling period, the

583   OH reactivity values of VOCs ($OH\ reactivity_{VOCs}$) were within the range of 33-123% of the

584   average $OH\ reactivity_{VOCs}$ during O_3 episodes. For OH reactivity of NO_x ($OH\ reactivity_{NOx}$),

585   the range was 61-242%. The O_3 production rates were simulated in a set of assumed scenarios

586   with different $OH\ reactivity_{VOCs}$ and $OH\ reactivity_{NOx}$ values. To include the OH reactivity

587   of VOCs and NO_x on all the VOC sampling days, factors from 10% to 140% with the step of 10%

588   were applied to the average diurnal profiles of VOCs and CO during O_3 episodes, while the

589   factors ranged from 10% to 300% with the step of 10% for NO_x. The initial concentrations of all

590   the air pollutants were also scaled by the factors and the model was constrained to these scaled

591   concentrations every hour, except for O_3. It should be noted that the factors applied to CO were

592   exactly the same as those applied to VOCs, therefore we use $VOCs^{\#}$ to represent the sum of

593   VOCs and CO hereafter. The 14 gradients of $OH\ reactivity_{VOCs^{\#}}$ values and 30 gradients of

594    $OH\ reactivity_{NOx}$ values made up 420 scenarios. Meteorological conditions were exactly the

595   same for all the scenarios and the clear sky was hypothesized. According to the simulations, the

596   maximum O_3 production rates occurred at 12:00 LT. Thus, the simulated O_3 production rates at

597   12:00 LT, as a function of percentages of $OH\ reactivity_{VOCs}$ and $OH\ reactivity_{NOx}$, are

598   plotted in Figure 8.

599

24
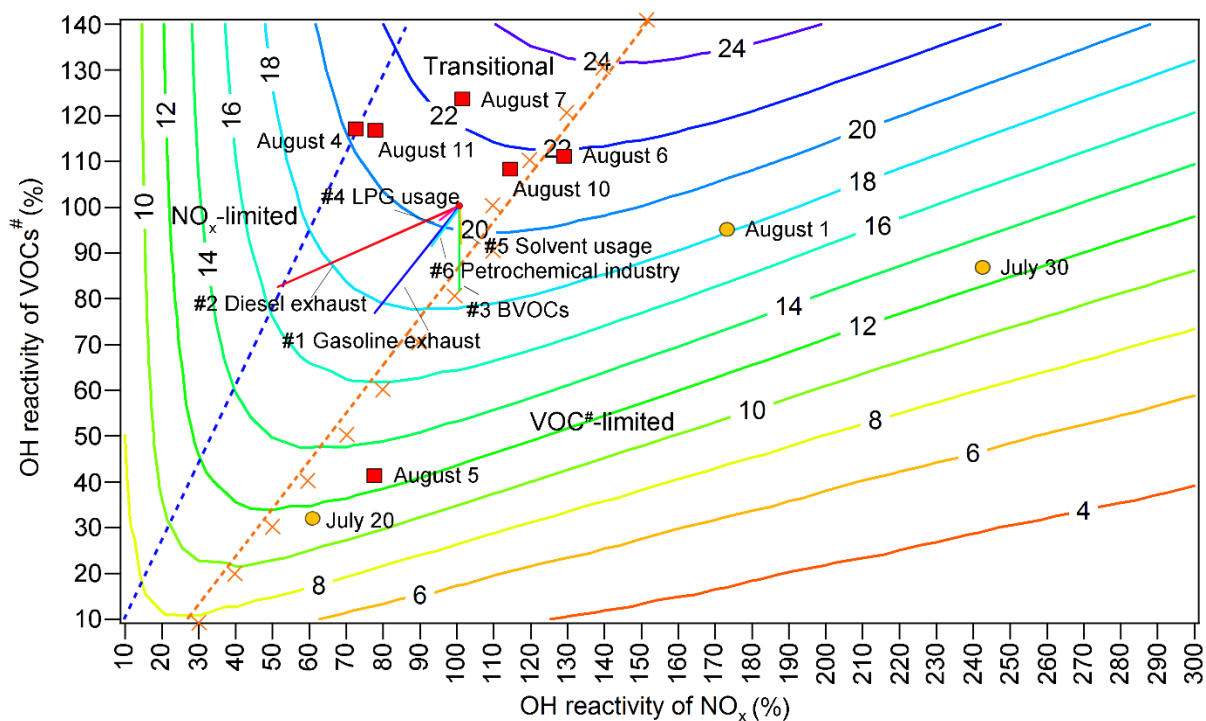
600 Figure 8 Isopleths of the net O_3 production rate (ppbv/hr) at 12:00 LT as a function of
601 $OH\ reactivity_{VOCs\#}$ and $OH\ reactivity_{NOx}$. The red blocks and orange circles denote the
602 calculated $OH\ reactivity_{VOCs\#}$ and $OH\ reactivity_{NOx}$ values at 12:00 LT on O_3 episode and
603 non-episode days, respectively. Each orange cross represents the $OH\ reactivity_{VOCs\#}$ and
604 $OH\ reactivity_{NOx}$ at 12:00 LT in the scenario with highest O_3 production rate at a given
605 $OH\ reactivity_{VOCs\#}$. The orange dashed line and blue dashed line divide O_3 formation into the
606 VOC-limited regime, transitional regime, and NO_x-limited regime.

607 Text S3 describes the methods to define the regimes of O_3 formation. Overall, O_3 formation was
608 mainly limited by VOCs[#] during non-episodes. However, it switched to be co-limited by VOCs[#]
609 and NO_x (transitional regime) on episode days with the net O_3 production rates among the
610 highest, except for August 5 when the strong sea breeze diluted air pollutants in Ji'nan and/or
611 intercepted the transport of air pollutants from Central China to Ji'nan (Figure S6). In fact, the
612 sensitivity of O_3 formation to NO_x might be underemphasized due to the positive biases of NO_2
613 measurement (Lu et al., 2010). This effect was expected to be more significant during episodes
614 when the overestimation of NO_2 was more obvious. However, O_3 formation was not likely only
615 limited by NO_x even during O_3 episodes, because NO_2 could not be overestimated by more than
616 30% according to our inferences (see section 2.2.1). Therefore, O_3 formation was treated to be in
617 the transitional regime during episodes. This partially explained the increased O_3 during episodes
618 in Ji'nan, given the higher O_3 production rates in transitional regime (Figure 8). Noticeably, the
619 change of regimes controlling O_3 formation is consistent with that predicted by the
620 $\frac{OH\ reactivity_{VOCs\#}}{OH\ reactivity_{NOx}}$ ratio and the ratio of the reaction rates between "HO_2+RO_2" and "$OH+NO_2$".

621 The source apportionment of O_3 precursors enabled us to calculate the source-specific
622 $OH\ reactivity_{VOCs\#}$ and $OH\ reactivity_{NOx}$ values. Accordingly, the variations of O_3
623 production rates induced by the reductions in source emissions are presented in Figure 8 (straight
624 solid lines #1-#6). The start point of the straight lines corresponded to 100% of the total average
625 $OH\ reactivity_{VOCs\#}$ and $OH\ reactivity_{NOx}$ during O_3 episodes. The end points, however,
626 represented the $OH\ reactivity_{VOCs\#}$ and $OH\ reactivity_{NOx}$ with the complete removal of
627 emissions from the individual sources. Therefore, the differences of the O_3 production rates
628 between the start point and end points were the source contributions to the O_3 production rates,

629 while the lengths of the lines reflected the contributions to the OH reactivity of the sources.

630 Further, the simulated O_3 production rates on the lines #1-#6, as a response of reductions in

631 source emissions, are extracted and plotted in Figure S14. Obviously, the highest efficiencies of

632 O_3 reduction could be achieved by cutting diesel exhaust (0.58 ppbv hr^{-1}/10% emission reduction)

633 and gasoline exhaust (0.47 ppbv hr^{-1}/10% emission reduction). In fact, the sensitivities of O_3

634 production rates to the vehicle exhausts might be somewhat underestimated, due to the exclusion

635 of carbonyls in the source apportionment. However, the reductions of O_3 production rates by

636 cutting 10% of vehicle exhausts were still insignificant, compared to the overall maximum O_3

637 production rate of 21.3 ppbv/hr during O_3 episodes. This indicated that by only restraining

638 emissions from one to two sources, high percentages of emission reductions were required to

639 sufficiently reduce the overall O_3 production rate. Otherwise, the combined efforts should be

640 made to control the emissions of O_3 precursors from the diverse sources. In particular, it is

641 essential to get rid of the transitional regime featuring high O_3 production rates.

4 Implications

643 This study investigates the causes of a severe O_3 pollution event lasting for eight consecutive

644 days in the NCP, one of the most densely populated regions in the world. Photochemical

645 formation in the lower troposphere of the NCP is demonstrated as the main source of O_3, under

646 the control of weak high pressure or low pressure trough. Though the emissions of NO_x, an

647 important precursor of O_3, have been significantly reduced in China since 2013 (Duncan et al.,

648 2016; Liu et al., 2017), O_3 pollution is still severe or even worsening in the NCP, as revealed in

649 the present and also previous studies (Zhang et al., 2014; Sun et al., 2016). The finding that O_3

650 formation shifted from VOC-limited regime on relatively low O_3 days to the transitional regime

651 on O_3 non-attainment days may elucidate the increase of O_3, because O_3 production rates in the

652 transitional regime are the highest. It is unrealistic to expect the continuously linear reduction in

653 NO_x emissions in the NCP, after the substantial decreases of emissions from power plants and

654 industries in recent years. In other words, restraining on VOC emissions is urgent for O_3

655 abatement in the NCP. Another important finding in this study is that the NCP served as an O_3

656 source. This was ever proposed by Ding et al. (2009), based on the aircraft measurement and

657 simulation of atmospheric dynamics. We confirm it through the ground-level observation and the

658 simulation of in-situ photochemistry. It can be expected that organic nitrates are also intensively

659 formed in the NCP as byproducts of O_3 formation. In view of the fact that the NCP locates

660 within the mid-latitude band of Northern Hemisphere under the dominance of westerlies, we

661 believe that O_3 and organic nitrates formed in this region may be transported over a long distance

662 following the uplifting of air masses, which has been confirmed to partially account for the

663 enhancement of background O_3 in North America and even Europe (Derwent et al., 2015; Lin et

664 al., 2017). Therefore, the recent air pollution control measures taken in China (including China's

665 Clean Air Act Plan in force in 2013) are still inadequate to ease the burden of global tropospheric

666 O_3 in a short period. More effective Action Plans should be implemented for O_3 benefit, with

667 comprehensive thinking of atmospheric dynamics and chemistry.

Author contribution

669 The study was designed by the corresponding author, Hai Guo, with the help of Lihui Han and

670 Ying Zhou. Fei Jiang and Hairong Cheng provided valuable input on the characteristics of

671 meteorological conditions and emissions of air pollutants in the NCP. Xiaopu Lyu collected the

672 samples and managed the logistics in the field campaign, when Likun Xue provided sufficient

673 assistances in field sampling campaign. The solar radiation data in Ji'nan were obtained from

674 Zhe Cai. Xiaopu Lyu did data analyses and wrote the paper, while the chemical transport

675 modelling was done by Nan Wang and Yangzong Zeren. Hai Guo revised and finalized the paper

676 for submission.

687

References

688

689 Atkinson, R.: Atmospheric chemistry of VOCs and NO_x, Atmos. Environ., 34, 2063-2101, **2000**.

690 Beck, J.P. and Grennfelt, P.: Estimate of ozone production and destruction over northwestern
691 Europe, Atmos. Environ., 28, 129-140, **1994**.

692 Cai, C., Geng, F., Tie, X., Yu, Q., and An, J.: Characteristics and source apportionment of VOCs
693 measured in Shanghai, China, Atmos. Environ., 44, 5005-5014, **2010**.

694 Carter, W.P.: Development of ozone reactivity scales for volatile organic compounds, Air &
695 Waste Manage. Assoc., 44, 881-899, **1994**.

696 Carter, W.P., Pierce, J.A., Luo, D., and Malkina, I.L.: Environmental chamber study of
697 maximum incremental reactivities of volatile organic compounds, Atmos. Environ., 29(18),
698 2499-2511, **1995**.

699 Chameides, W. and Walker, J.C.: A photochemical theory of tropospheric ozone, J. Geophys.
700 Res., 78(36), 8751-8760, **1973**.

701 Chan, C.Y. and Chan, L.Y.: Effect of meteorology and air pollutant transport on ozone episodes
702 at a subtropical coastal Asian city, Hong Kong, J. Geophys. Res. − Atmos., 105(D16), 20707-
703 20724, **2000**.

704 Chen, Y., Zhao, C., Zhang, Q., Deng, Z., Huang, M., and Ma, X.: Aircraft study of mountain
705 chimney effect of Beijing, China, J. Geophys. Res. − Atmos., 114(D8),
706 doi:10.1029/2008JD010610, **2009**.

707 Cheng, H., Guo, H., Wang, X., Saunders, S.M., Lam, S.H.M., Jiang, F., Wang, T., Ding, A., Lee,
708 S., and Ho, K.F.: On the relationship between ozone and its precursors in the Pearl River Delta:
709 application of an observation-based model (OBM), Environ. Sci. Pollut. Res., 17(3), 547-560,
710 **2010**.

711 Colman, J.J., Swanson, A.L., Meinardi, S., Sive, B.C., Blake, D.R., and Rowland, F.S.:
712 Description of the analysis of a wide range of volatile organic compounds in whole air samples
713 collected during PEM-Tropics A and B, Anal. Chem., 73(15), 3723-3731, **2001**.

Cooper, O.R., Stohl, A., Hübler, G., Hsie, E.Y., Parrish, D.D., Tuck, A.F., Kiladis, G.N., Oltmans, S.J., Johnson, B.J., Shapiro, M., and Moody, J.L.: Direct transport of midlatitude stratospheric ozone into the lower troposphere and marine boundary layer of the tropical Pacific Ocean, J. Geophys. Res.: Atmos., 110(D23), **2005**.

Crutzen, P.: A discussion of the chemistry of some minor constituents in the stratosphere and troposphere, Pure Appl. Geophys., 106(1), 1385-1399, **1973**.

Derwent, R.G., Utembe, S.R., Jenkin, M.E., and Shallcross, D.E.: Tropospheric ozone production regions and the intercontinental origins of surface ozone over Europe, Atmos. Environ., 112, 216-224, **2015**.

Ding, A.J., Fu, C.B., Yang, X.Q., Sun, J.N., Zheng, L.F., Xie, Y.N., Herrmann, E., Nie, W., Petaja, T., Kerminen, V.M., and Kulmala, M.: Ozone and fine particle in the western Yangtze River Delta: an overview of 1 yr data at the SORPES station, Atmos. Chem. Phys., 13(11):5813-30, **2013**.

Ding, A., Wang, T., Xue, L., Gao, J., Stohl, A., Lei, H., Jin, D., Ren, Y., Wang, X., Wei, X., and Qi, Y.: Transport of north China air pollution by midlatitude cyclones: Case study of aircraft measurements in summer 2007, J. Geophys. Res.: Atmos., 114(D8), **2009**.

Duncan, B.N., Lamsal, L.N., Thompson, A.M., Yoshida, Y., Lu, Z., Streets, D.G., Hurwitz, M.M., and Pickering, K.E.: A space-based, high-resolution view of notable changes in urban NO_x pollution around the world (2005-2014), J. Geophys. Res.: Atmos., 121(2), 976-996, **2016**.

Dunlea, E.J., Herndon, S.C., Nelson, D.D., Volkamer, R.M., San Martini, F., Sheehy, P.M., Zahniser, M.S., Shorter, J.H., Wormhoudt, J.C., Lamb, B.K., and Allwine, E.J.: Evaluation of nitrogen dioxide chemiluminescence monitors in a polluted urban environment, Atmos. Chem. Phys., 7(10), 2691-2704, **2007**.

Finlayson-Pitts, B.J., and Pitts Jr, J.N.: Atmospheric chemistry of tropospheric ozone formation: scientific and regulatory implications, Air & Waste Manage. Assoc., 43(8), 1091-1100, **1993**.

Fung, J.C.H., Lau, A.K.H., Lam, J.S.L., and Yuan, Z.: Observational and modeling analysis of a severe air pollution episode in western Hong Kong, J. Geophys. Res. – Atmos., 110(D9), **2005**.

Gao, J., Wang, T., Ding, A., and Liu, C.: Observational study of ozone and carbon monoxide at the summit of mount Tai (1534m asl) in central-eastern China, Atmos. Environ., 39(26), 4779-4791, **2005**.

Granby, K., Christensen, C.S., and Lohse, C.: Urban and semi-rural observations of carboxylic acids and carbonyls, Atmos. Environ., 31(10), 1403-1415, **1997**.

Grosjean, D., Miguel, A.H., and Tavares, T.M.: Urban air pollution in Brazil: Acetaldehyde and other carbonyls, Atmos. Environ., 24(1), 101-106, **1990**.

Gu, D., Wang, Y., Smeltzer, C., and Boersma, K.F.: Anthropogenic emissions of NO_x over China: Reconciling the difference of inverse modeling results using GOME-2 and OMI measurements. J. Geophys. Res.: Atmos., 119(12):7732-40, **2014**.

Guo, H., Ling, Z.H., Cheung, K., Jiang, F., Wang, D.W., Simpson, I.J., Barletta, B., Meinardi, S., Wang, T.J., Wang, X.M., Saunders, S.M., and Blake, D.R.: Characterization of photochemical pollution at different elevations in mountainous areas in Hong Kong, Atmos. Chem. Phys., 13(8), 3881-3898, **2013**.

Han, X., Zhu, L., Wang, S., Meng, X., Zhang, M., and Hu, J.: Modeling study of impacts on surface ozone of regional transport and emissions reductions over North China Plain in summer 2015, Atmos. Chem. Phys., 18(16):12207-21, **2018**.

He, J., Wang, Y., Hao, J., Shen, L., and Wang, L.: Variations of surface O_3 in August at a rural site near Shanghai: influences from the West Pacific subtropical high and anthropogenic emissions, Environ. Sci. Pollut. Res., 19(9), 4016-4029, **2012**.

He, K.: Multi-resolution Emission Inventory for China (MEIC): model framework and 1990-2010 anthropogenic emissions, In AGU Fall Meeting Abstracts, December, **2012**.

Huang, J.P., Fung, J.C., Lau, A.K., and Qin, Y.: Numerical simulation and process analysis of typhoon-related ozone episodes in Hong Kong, J. Geophys. Res. – Atmos., 110(D5), **2005**.

Jenkin, M.E. and Clemitshaw, K.C.: Ozone and other secondary photochemical pollutants: chemical processes governing their formation in the planetary boundary layer, Atmos. Environ., 34(16), 2499-2527, **2000**.

768   Jenkin, M.E., Saunders, S.M., and Pilling, M.J.: The tropospheric degradation of volatile organic

769   compounds: a protocol for mechanism development, Atmos. Environ., 31(1), 81-104, **1997**.

770   Jiang, F., Guo, H., Wang, T.J., Cheng, H.R., Wang, X.M., Simpson, I.J., Ding, A.J., Saunders,

771   S.M., Lam, S.H.M., and Blake, D.R.: An ozone episode in the Pearl River Delta: Field

772   observation and model simulation, J. Geophys. Res. – Atmos., 115(D22), **2010**.

773   Jin, X., Fiore, A.M., Murray, L.T., Valin, L.C., Lamsal, L.N., Duncan, B., Folkert Boersma, K.,

774   De Smedt, I., Abad, G.G., Chance, K., and Tonnesen, G.S.: Evaluating a Space-Based Indicator

775   of Surface Ozone-NO_x-VOC Sensitivity Over Midlatitude Source Regions and Application to

776   Decadal Trends, J. Geophys. Res.: Atmos., 122(19), **2017**.

777   Kanaya, Y., Pochanart, P., Liu, Y., Li, J., Tanimoto, H., Kato, S., Suthawaree, J., Inomata, S.,

778   Taketani, F., Okuzawa, K., and Kawamura, K.: Rates and regimes of photochemical ozone

779   production over Central East China in June 2006: a box model analysis using comprehensive

780   measurements of ozone precursors, Atmos. Chem. Phys., 9(20), 7711-7723, **2009**.

781   Kleinman, L.I.: The dependence of tropospheric ozone production rate on ozone precursors,

782   Atmos. Environ., (3), 575-586, **2005**.

783   Kusaka, H. and Kimura, F.: Coupling a single-layer urban canopy model with a simple

784   atmospheric model: Impact on urban heat island simulation for an idealized case, J. Meteoro. Soc.

785   Japan: Ser. II, 82(1), 67-80, **2004**.

786   Lam, S.H.M., Saunders, S.M., Guo, H., Ling, Z.H., Jiang, F., Wang, X.M., and Wang, T.J.:

787   Modelling VOC source impacts on high ozone episode days observed at a mountain summit in

788   Hong Kong under the influence of mountain-valley breezes, Atmos. Environ., 81, 166-176, **2013**.

789   Lang, J., Zhang, Y., Zhou, Y., Cheng, S., Chen, D., Guo, X., Chen, S., Li, X., Xing, X., and

790   Wang, H.: Trends of $PM_{2.5}$ and chemical composition in Beijing, 2000–2015, Aerosol Air Qual.

791   Res., 17, 412-425, **2017**.

792   Li, M., Zhang, Q., Kurokawa, J.I., Woo, J.H., He, K., Lu, Z., Ohara, T., Song, Y., Streets, D.G.,

793   Carmichael, G.R., and Cheng, Y.: MIX: a mosaic Asian anthropogenic emission inventory under

794   the international collaboration framework of the MICS-Asia and HTAP, Atmos. Chem. Phys.,

795   17(2), **2017**.

796 Lin, M., Fiore, A.M., Horowitz, L.W., Langford, A.O., Oltmans, S.J., Tarasick, D., and Rieder,
797 H.E.: Climate variability modulates western US ozone air quality in spring via deep stratospheric
798 intrusions, Nat. Commun., 6:7105, **2015**.

799 Lin, M., Horowitz, L.W., Payton, R., Fiore, A.M., and Tonnesen, G.: US surface ozone trends
800 and extremes from 1980 to 2014: quantifying the roles of rising Asian emissions, domestic
801 controls, wildfires, and climate, Atmos. Chem. Phys., 17(4), 2943-2970, **2017**.

802 Lin, W., Xu, X., Zhang, X., and Tang, J.: Contributions of pollutants from North China Plain to
803 surface ozone at the Shangdianzi GAW Station, Atmos. Chem. Phys., 8(19), 5889-5898, **2008**.

804 Liu, F., Beirle, S., Zhang, Q., Zheng, B., Tong, D., and He, K.: NO_x emission trends over
805 Chinese cities estimated from OMI observations during 2005 to 2015, Atmospheric chemistry
806 and physics, 17(15), 9261-9275, **2017**.

807 Liu, X.H., Zhang, Y., Xing, J., Zhang, Q., Wang, K., Streets, D.G., Jang, C., Wang, W.X., and
808 Hao, J.M.: Understanding of regional air pollution over China using CMAQ, part II. Process
809 analysis and sensitivity of ozone and particulate matter to precursor emissions, Atmos. Environ.,
810 44(30), 3719-3727, **2010**.

811 Lo, J.C., Lau, A.K., Fung, J.C., and Chen, F.: Investigation of enhanced cross‐city transport and
812 trapping of air pollutants by coastal and urban land‐sea breeze circulations, J. Geophys. Res. –
813 Atmos., 111(D14), **2006**.

814 Lyu, X.P., Chen, N., Guo, H., Zhang, W.H., Wang, N., Wang, Y., and Liu, M.: Ambient volatile
815 organic compounds and their effect on ozone production in Wuhan, central China, Sci. Total
816 Environ., 541:200-9, **2016**.

817 Lyu, X.P., Guo, H., Wang, N., Simpson, I.J., Cheng, H.R., Zeng, L.W., Saunders, S.M., Lam, S.
818 H.M., Meinardi, S., and Blake, D.R.: Modeling C_1-C_4 alkyl nitrate photochemistry and their
819 impacts on O_3 production in urban and suburban environments of Hong Kong, J. Geophys. Res.
820 – Atmos., 122(19), **2017**.

821 Lu, K., Zhang, Y., Su, H., Brauers, T., Chou, C.C., Hofzumahaus, A., Liu, S.C., Kita, K., Kondo,
822 Y., Shao, M., and Wahner, A.: Oxidant (O_3 + NO_2) production processes and formation regimes
823 in Beijing, J. Geophys. Res.: Atmos., 115(D7), **2010**.

824 Madronich, S. and Flocke, S.: Theoretical estimation of biologically effective UV radiation at the

825 Earth's surface, In Solar Ultraviolet Radiation (pp. 23-48), Springer, Berlin, Heidelberg, **1997**.

826 Mao, J., Ren, X., Chen, S., Brune, W.H., Chen, Z., Martinez, M., Harder, H., Lefer, B.,

827 Rappenglueck, B., Flynn, J., and Leuchner, M.: Atmospheric oxidation capacity in the summer

828 of Houston 2006: Comparison with summer measurements in other metropolitan studies, Atmos.

829 Environ., 44(33), 4107-4115, **2010**.

830 McClenny, W.A., Williams, E.J., Cohen, R.C., and Stutz, J.: Preparing to measure the effects of

831 the NO_x SIP Call—methods for ambient air monitoring of NO, NO_2, NO_y, and individual NO_z

832 species, Air & Waste Manage. Assoc,, 52(5), 542-562, **2002**.

833 Monks, P. S.: Gas-phase radical chemistry in the troposphere, Chem. Soc. Reviews, 34(5), 376-

834 395, **2005**.

835 Ren, X., Harder, H., Martinez, M., Lesher, R.L., Oliger, A., Simpas, J.B., Brune, W.H., Schwab,

836 J.J., Demerjian, K.L., He, Y., and Zhou, X.: OH and HO_2 chemistry in the urban atmosphere of

837 New York City, Atmos. Environ., 37(26), 3639-3651, **2003**.

838 Saunders, S.M. Jenkin, M.E., Derwent, R.G., and Pilling, M.J.: Protocol for the development of

839 the Master Chemical Mechanism, MCM v3 (Part A): tropospheric degradation of non-aromatic

840 volatile organic compounds, Atmos. Chem. Phys., 3(1), 161-180, **2003**.

841 Shan, W., Yin, Y., Zhang, J., and Ding, Y.: Observational study of surface ozone at an urban site

842 in East China, Atmos. Res., 89(3), 252-261, **2008**.

843 Shao, M., Lu, S., Liu, Y., Xie, X., Chang, C., Huang, S., and Chen, Z.: Volatile organic

844 compounds measured in summer in Beijing and their role in ground-level ozone formation, J.

845 Geophys. Res. – Atmos., 114(D2), doi.org/10.1029/2008JD010863, **2009b**.

846 Shu, L., Xie, M., Wang, T., Gao, D., Chen, P., Han, Y., Li, S., Zhuang, B., and Li, M.: Integrated

847 studies of a regional ozone pollution synthetically affected by subtropical high and typhoon

848 system in the Yangtze River Delta region, China, Atmos. Chem. Phys., 16(24), 15801-15819,

849 **2016**.

850 Sillman, S.: The relation between ozone, NO_x and hydrocarbons in urban and polluted rural

851 environments, Atmos. Environ., 33(12), 1821-1845, **1999**.

852 Sun, L., Xue, L., Wang, T., Gao, J., Ding, A., Cooper, O.R., Lin, M., Xu, P., Wang, Z., Wang, X.,

853 Wen, L., Zhu, Y., Chen, T., Yang, L., Wang, Y., Chen, J., and Wang, W.: Significant increase of

854 summertime ozone at Mount Tai in Central Eastern China, Atmos. Chem. Phys., 16(16), 10637-

855 10650, **2016**.

856 Tan, Z., Lu, K., Dong, H., Hu, M., Li, X., Liu, Y., Lu, S., Shao, M., Su, R., Wang, H., and Wu,

857 Y.: Explicit diagnosis of the local ozone production rate and the ozone-NO_x-VOC sensitivities,

858 Sci. Bull., 63(16):1067-76, **2018**.

859 Tan, Z., Lu, K., Jiang, M., Su, R., Dong, H., Zeng, L., Xie, S., Tan, Q., and Zhang, Y.: Exploring

860 ozone pollution in Chengdu, southwestern China: A case study from radical chemistry to O_3-

861 VOC-NO_x sensitivity, Sci. Total Environ., 636:775-86, **2018**.

862 Thornton, J.A., Wooldridge, P.J., Cohen, R.C., Martinez, M., Harder, H., Brune, W.H., Williams,

863 E.J., Roberts, J.M., Fehsenfeld, F.C., Hall, S.R., and Shetter, R.E.: Ozone production rates as a

864 function of NO_x abundances and HO_x production rates in the Nashville urban plume, J. Geophys.

865 Res. – Atmos., 107(D12), doi.org/10.1029/2001JD000932, **2002**.

866 Wang, N., Guo, H., Jiang, F., Ling, Z. H., and Wang, T.: Simulation of ozone formation at

867 different elevations in mountainous area of Hong Kong using WRF-CMAQ model, Sci. Total

868 Environ., 505, 939-951, **2015b**.

869 Wang, T., Ding, A., Gao, J., and Wu, W.S.: Strong ozone production in urban plumes from

870 Beijing, China, Geophys. Res. Lett., 33(21), **2006**.

871 Wang, T., Nie, W., Gao, J., Xue, L.K., Gao, X.M., Wang, X.F., Qiu, J., Poon, C.N., Meinardi, S.,

872 Blake, D., Wang, S.L., Ding, A.J., Chai, F.H., Zhang, Q.Z., and Wang, W.X.: Air quality during

873 the 2008 Beijing Olympics: secondary pollutants and regional impact, Atmos. Chem. Phys.,

874 10(16), 7603-7615, **2010**.

875 Wang, X.M., Lin, W.S., Yang, L.M., Deng, R.R., and Lin, H.: A numerical study of influences

876 of urban land‐use change on ozone distribution over the Pearl River Delta region, China, Tellus

877 B, 59(3), 633-641, **2007**.

878 Wang, Z., Li, Y., Chen, T., Zhang, D., Sun, F., Wei, Q., Dong, X., Sun, R., Huan, N., and Pan, L.:

879 Ground-level ozone in urban Beijing over a 1-year period: Temporal variations and relationship

880 to atmospheric oxidation, Atmos. Res., 164, 110-117, **2015a**.

881 Whitten, G.Z., Heo, G., Kimura, Y., McDonald-Buller, E., Allen, D.T., Carter, W.P., and
882 Yarwood, G.: A new condensed toluene mechanism for Carbon Bond: CB05-TU, Atmos.
883 Environ., 44(40), 5346-5355, **2010**.

884 Williams, J., Keßel, S.U., Nölscher, A.C., Yang, Y., Lee, Y., Yáñez-Serrano, A.M., Wolff, S.,
885 Kesselmeier, J., Klüpfel, T., Lelieveld, J., and Shao, M.: Opposite OH reactivity and ozone
886 cycles in the Amazon rainforest and megacity Beijing: Subversion of biospheric oxidant control
887 by anthropogenic emissions, Atmos. Environ., 125, 112-118, **2016**.

888 Xing, C., Liu, C., Wang, S., Chan, K.L., Gao, Y., Huang, X., Su, W., Zhang, C., Dong, Y., Fan,
889 G., and Zhang, T.: Observations of the vertical distributions of summertime atmospheric
890 pollutants and the corresponding ozone production in Shanghai, China, Atmos. Chem. Phys.,
891 17(23), **2017**.

892 Xing, J., Ding, D., Wang, S., Zhao, B., Jang, C., Wu, W., Zhang, F., Zhu, Y., and Hao, J.:
893 Quantification of the enhanced effectiveness of NO_x control from simultaneous reductions of
894 VOC and NH_3 for reducing air pollution in the Beijing–Tianjin–Hebei region, China, Atmos.
895 Chem. Phys., 18(11):7799-814, **2018**.

896 Xu, Z., Wang, T., Xue, L.K., Louie, P.K., Luk, C.W., Gao, J., Wang, S.L., Chai, F.H., and Wang,
897 W.X.: Evaluating the uncertainties of thermal catalytic conversion in measuring atmospheric
898 nitrogen dioxide at four differently polluted sites in China, Atmos. Environ., 76, 221-226, **2013**.

899 Xue, L.K., Wang, T., Gao, J., Ding, A.J., Zhou, X.H., Blake, D.R., Wang, X.F., Saunders, S.M.,
900 Fan, S.J., Zuo, H.C., Zhang, Q.Z. and Wang, W.X.: Ground-level ozone in four Chinese cities:
901 precursors, regional transport and heterogeneous processes, Atmos. Chem. Phys., 14(23), 13175-
902 13188, **2014**.

903 Yang, Y., Shao, M., Wang, X., Nolscher, A.C., Kessel, S., Guenther, A., and Williams, J.:
904 Towards a quantitative understanding of total OH reactivity: A review, Atmos. Environ.,
905 134:147-161, **2016**.

906 Ye, L., Wang, X., Fan, S., Chen, W., Chang, M., Zhou, S., Wu, Z., and Fan, Q.: Photochemical
907 indicators of ozone sensitivity: application in the Pearl River Delta, China, Front. Env. Sci. Eng.
908 10(6):15, **2016**.

909 Yin, Y., Lu, H., Shan, W., and Zheng, Y.: Analysis of observed ozone episode in urban Jinan,
910 China, Bulletin Environ. Contamination & toxico., 83(2), 159-163, **2009**.

911 Zhang, Q., Streets, D.G., Carmichael, G.R., He, K.B., Huo, H., Kannari, A., Klimont, Z., Park,
912 I.S., Reddy, S., Fu, J.S., Chen, D., Duan, L., Lei, Y., Wang, L.T., and Yao, Z.L.,: Asian
913 emissions in 2006 for the NASA INTEX-B mission, Atmos. Chem. Phys., 9(14), 5131-5153,
914 **2009**.

915 Zhang, Q., Streets, D.G., He, K., Wang, Y., Richter, A., Burrows, J.P., Uno, I., Jang, C.J., Chen,
916 D., Yao, Z., and Lei, Y.: NO_x emission trends for China, 1995-2004: The view from the ground
917 and the view from space, J. Geophys. Res. – Atmos., 112(D22), **2007**.

918 Zhang, Q., Yuan, B., Shao, M., Wang, X., Lu, S., Lu, K., Wang, M., Chen, L., Chang, C.C., and
919 Liu, S.C.: Variations of ground-level O_3 and its precursors in Beijing in summertime between
920 2005 and 2011, Atmos. Chem. Phys., 14(12), 6089-6101, **2014**.

921 Zhang, Y., Ding, A., Mao, H., Nie, W., Zhou, D., Liu, L., Huang, X., and Fu, C.: Impact of
922 synoptic weather patterns and inter-decadal climate variability on air quality in the North China
923 Plain during 1980-2013, Atmos. Environ., 124, 119-128, **2016**.

924 Zhang, Z., Zhang, X., Gong, D., Quan, W., Zhao, X., Ma, Z., and Kim, S.J.: Evolution of surface
925 O_3 and $PM_{2.5}$ concentrations and their relationships with meteorological conditions over the last
926 decade in Beijing, Atmos. Environ., 108, 67-75, **2015**.

927 Zhao, C., Wang, Y., and Zeng, T.: East China plains: A "basin" of ozone pollution, Environ. Sci.
928 Technol., 43(6), 1911-1915, **2009**.

929 Zong, R., Yang, X., Wen, L., Xu, C., Zhu, Y., Chen, T., Yao, L., Wang, L., Zhang, J., Yang, L.,
930 Wang, X., Shao, M., Zhu, T., Xue, L., and Wang, W.: Strong ozone production at a rural site in
931 the North China Plain: Mixed effects of urban plumes and biogenic emissions, J. Environ. Sci.,
932 doi.org/10.1016/j.jes.2018.05.003, **2018**.